Journal of Petroleum Science and Engineering 111 (2013) 1–14

Contents lists available at ScienceDirect

Journal of Petroleum Science and Engineering

journal homepage: www.elsevier.com/locate/petrol

Simulation of slug flow systems under laminar regime: Hydrodynamics with individual and a pair of consecutive Taylor bubbles

J.D.P. Araújo *, J.M. Miranda, J.B.L.M. Campos

Centro de Estudos de Fenómenos de Transporte, Departamento de Engenharia Química, Universidade do Porto, Faculdade de Engenharia, Rua Dr. Roberto Frias, 4200-465 Porto, Portugal

ARTICLE INFO

Article history:
Received 31 March 2013
Accepted 2 October 2013
Available online 11 October 2013

Keywords:
slug flow
CFD
gas–oil flow
Taylor bubble velocity
wake region
bubble–bubble interaction

ABSTRACT

Introduction: Slug flow is an extremely important gas–liquid flow pattern that can be frequently found in oil extraction processes causing instabilities and randomness in the hydrodynamic environment of an oil well.

Methods: The dynamics of individual and a pair of Taylor bubbles rising in vertical columns of stagnant and co-current liquids was numerically studied using the volume of fluid (VOF) methodology implemented in the commercial code ANSYS FLUENT. The first step was to validate the application of the numerical code to slug flow with in-house experimental data about the rising of single Taylor bubbles obtained by photographic studies and PIV/PST measurements. Then, the application of this CFD tool was extended to a system with a pair of Taylor bubbles.

Results: The numerical results of the single Taylor bubble velocity, frontal bubble shape, liquid film thickness, wall shear stress in the stabilized film, axial velocity in the liquid film, bubble shape at the rear, wake volume and length are favorably compared with available experimental and theoretical values. Regarding systems with a pair of consecutive Taylor bubbles, which are the structural units of continuous slug flow, the hydrodynamics was simulated under stagnant and co-current liquid flow conditions, with physical properties that can be representative of some gas–oil systems. The behavior of the most important hydrodynamic features, as the bubbles approach process evolves, is addressed to infer the major effects caused by this kind of bubble–bubble interaction.

Conclusions: The information gathered about the bubble–bubble interaction can be crucial to improve already developed bubble train flow simulators.

1. Introduction

Multiphase flows occur in a wide range of industrial scenarios, and their characterization is crucial for proper modeling, design and operation of several process units. One of the most relevant of these scenarios is oil fields, where multiphase flows through deep wells are involved (Brill and Mukherjee, 1999). Particularly problematic are the intermittent flow patterns, such as slug flow, since it introduces instability and randomness to pressure drop and heat and mass transfer coefficients along the oil wells, or in severe slugging situations, the flooding and over-pressurization caused may lead to a complete shutdown of a facility or even the abandonment of the well (Malekzadeh et al., 2012).

The complex structure of slug flow is frequently simplified as a sequence of "fundamental units". Each unit comprises an elongated bullet-shaped bubble (usually above 2–3 tube diameters long) that fills almost the entire pipe cross section, known as Taylor bubbles, a liquid film flowing downwards between the bubble interface and the pipe wall, and a portion of liquid below the bubble bottom that usually contains a recirculation zone. Besides its frequent occurrence in oil wells, slug flow can also be encountered in several other industrial and practical situations, such as volcanic phenomena (James et al., 2004); enhancement of ultrafiltration processes by injection of Taylor bubbles to improve the cleaning effects and avoid concentration polarization of the membrane surface (Mercier et al., 1997; Taha and Cui, 2002); increase of heat and mass transfer in multiphase reactor systems (Pangarkar et al., 2008); gas embolism, which occurs when air enters the human vascular structures causing morbidity or death (Branger et al., 2001; Chung et al., 2007); and microflow systems (Angeli and Gavriilidis, 2008; Talimi et al., 2012).

The characteristics of a hydrodynamic environment such as slug flow are dependent on the interaction between gravitational, interfacial, viscous and inertial forces. Performing a dimensional analysis to this kind of systems, the problem can be reduced to the

* Corresponding author. Tel.: +351 22 508 1692.
E-mail addresses: daraujo@fe.up.pt (J.D.P. Araújo), jmiranda@fe.up.pt (J.M. Miranda), jmc@fe.up.pt (J.B.L.M. Campos).

0920-4105/$ - see front matter © 2013 Elsevier B.V. All rights reserved.
http://dx.doi.org/10.1016/j.petrol.2013.10.007

role of three dimensionless groups: Morton number or property group (M); Eötvös number that quantifies the ratio between surface and gravitational forces (Eo); and Froude number defined by the ratio of inertial and gravitational forces (Fr). These dimensionless groups are expressed by the following expressions:

$$M = \frac{g\mu_L^4(\rho_L - \rho_G)}{\rho_L^2\sigma^3} \quad (1)$$

$$Eo = \frac{g(\rho_L - \rho_G)D^2}{\sigma} \quad (2)$$

$$Fr = \frac{U_{SB}}{\sqrt{gD(\rho_L - \rho_G)/\rho_L}} \quad (3)$$

where ρ_L and ρ_G are the liquid and gas density, respectively, D the tube diameter, σ the surface tension, μ_L the dynamic viscosity of the liquid, and U_{SB} the Taylor bubble velocity.

Another relevant dimensionless group is the inverse viscosity number, $N_f = \rho_L\sqrt{gD^3}/\mu_L$, that can be derived from manipulation of Morton and Eötvös numbers, $N_f = (Eo^3/M)^{1/4}$.

Since the publication of some classic and pioneering works (Dumitrescu, 1943; Davies and Taylor, 1950; Goldsmith and Mason, 1962; White and Beardmore, 1962), a significant amount of research has been dedicated to understand the complexity of slug flow. Regarding the study and modeling of continuous slug flow applied to oil and geothermal wells, several works have been presented in the last 20 years, with different kinds of approaches and features involved (Barnea and Taitel, 1993; van Hout et al., 2001; Zhang et al., 2003; Mayor et al., 2007a, 2007b; Xia et al., 2009; Hasan and Kabir, 2010a, 2010b; Livescu et al., 2010; Choi et al., 2013). From the models/simulators of the referred studies, those which were made to produce numerical data for velocity and slug length distributions along the well (Barnea and Taitel, 1993; van Hout et al., 2001; Mayor et al., 2007a, 2007b; Xia et al., 2009) are better suited to predict the hydrodynamics of the developing state of continuous slug flow, i.e., follow the increase on slug length, not only due to expansion phenomenon, but essentially due to bubble–bubble interaction and coalescence. However, the main input for these slug flow tracking simulators is some information that describes the interaction between consecutive bubbles as a function of the separation distance. To obtain this crucial information, it is necessary to study with detail the systems composed by "fundamental units" of slug flow.

Several experimental studies about the flow of individual Taylor bubbles through liquids inside vertical columns are worth to mention (Campos and Guedes de Carvalho, 1988; Clanet et al., 2004; Liberzon et al., 2006; Nogueira et al., 2006a, 2006b; Shemer et al., 2007a). The coalescence mechanism of pairs of consecutive Taylor bubbles in vertical pipes is a research subject that is not yet been sufficiently explored. The first publication on this topic goes back to the work carried out by Moissis and Griffith (1962), and since then only a small number of studies have been reported about the flow of pairs of Taylor bubbles (Pinto and Campos, 1996; Pinto et al., 1998; Aladjem Talvy et al., 2000; Shemer et al., 2007b; Sousa et al., 2007). Within these studies, it is possible to find information about the bubbles shape and rising velocities, in systems with stagnant and co-currently flowing Newtonian and non-Newtonian liquids within a wide range of viscosities. The experimental methods applied include pressure transducer taps to determine bubbles velocities (Pinto and Campos, 1996; Pinto et al., 1998), video imaging solely (Aladjem Talvy et al., 2000) or coupled with PIV techniques (Shemer et al., 2007b), and sets of laser diodes/photocells (Sousa et al., 2007).

Despite the importance of the information compiled so far through experimental research about the flow of single and pairs of Taylor bubbles, the complexity of the hydrodynamics involved requires methods able to complement some limitations of experimental techniques. Over the last years, computational tools revealed to be very useful on tackling those limitations by producing high precision data about the hydrodynamic features of systems with individual Taylor bubbles (Clarke and Issa, 1997; Kawaji et al., 1997; Bugg et al., 1998; Ha-Ngoc and Fabre, 2006; Taha and Cui, 2006; Feng, 2008; Lu and Prosperetti, 2009; Kang et al., 2010; Araújo et al., 2012).

Regarding the hydrodynamics of the flow of two consecutive Taylor bubbles, there is not yet any relevant CFD study published on this topic. The only numerical information found that is closer to this topic regards the coalescence of shorter bubbles in narrow vertical tubes (Farhangi et al., 2010).

In this work it is intended to clearly demonstrate and explore the capabilities of CFD tools on describing the dynamics of slug flow systems consisting on individual and pairs of Taylor bubbles rising through vertical columns of stagnant and co-current Newtonian liquids, and show the utility of the produced data as a preliminary step to the description and prediction of some multiphase flow phenomena occurring in oil wells. In practical terms, the idea is to use these CFD tools to complement and extend models/simulators proper for very long columns (Barnea and Taitel, 1993; van Hout et al., 2001; Zhang et al., 2003; Mayor et al., 2007a, 2007b; Xia et al., 2009; Hasan and Kabir, 2010a, 2010b; Livescu et al., 2010; Choi et al., 2013) by producing numerical information taken in smaller domains (enough length to include two consecutive Taylor bubbles and corresponding liquid surroundings), and so, adding or improving features regarding bubble–bubble interaction to these models/simulators. This work is also a starting point for research to perform in short-term future since it addresses systems under laminar regime, and though this kind of systems have a considerable relevance, it is a fact that the turbulent regime predominates on a wider spectrum of flow conditions occurring inside oil wells.

Firstly, the application of the numerical code to simulate slug flow was validated, where some flow conditions already tested experimentally for individual Taylor bubbles were replicated. The obtained numerical data was favorably compared with the available experimental data on the flow above the bubble nose region, liquid film (Nogueira et al., 2006a) and wake region (Campos and Guedes de Carvalho, 1988; Nogueira et al., 2006b). Afterwards, the same physical properties of the liquid and gas phases of one of the referred flow conditions, corresponding to a Morton number of 4.31×10^{-2} and Eo around 186, were used in two simulations involving the rising of a pair of consecutive Taylor bubbles: one in a stagnant vertical column of liquid; and the other with the liquid phase flowing co-currently at an average velocity (U_{SL}) of 0.2 m/s. The behavior of the most relevant hydrodynamic features with the separation distance between bubbles is then presented.

This CFD application can motivate considerable interest due to some important reasons: the absence of numerical research about the phenomena involved in the mechanism of approach and imminence of coalescence of two Taylor bubbles; higher spatial and temporal definition of CFD data and the inability of experimental techniques to produce accurate data when the separation distances between bubbles is very small; and the relevance of better understanding and modeling processes that involve continuous slug flow, particularly in the petroleum industry, based on reliable data produced for their "fundamental units", i.e., systems with pairs of consecutive Taylor bubbles. In the case of this work, the order of magnitude of M and Eo applied in the two simulations with a pair of consecutive Taylor bubbles can also be obtained in some real gas–oil systems, more precisely when the liquid phase is characterized by an API gravity somewhat lower than 20 and a viscosity around 0.1 Pa s, i.e., when dealing with a heavy crude oil according to the classification of De Ghetto et al. (1994).

2. CFD model

The flow of single and a pair of consecutive Taylor bubbles through stagnant and co-current Newtonian liquids was simulated with the commercial CFD package ANSYS FLUENT (Release 12.0.1). This package already includes the volume of fluid (VOF) method (Hirt and Nichols, 1981), which was the interface capturing technique applied, together with the geometric reconstruction scheme (Youngs, 1982) that assumes a piecewise-linear approach in the representation of the interface between phases.

The surface tension model applied in the ANSYS FLUENT package is the continuum surface force model (Brackbill et al., 1992). The surface tension effects, along the gas–liquid interface, are included into the VOF model through a source term in the momentum equation.

A two-dimensional coordinate system with axial symmetry around the tube centerline was used in order to avoid excessive time-consuming simulations and minimize the computational effort. This simplification is valid because, in this work, the values of the inverse viscosity dimensionless number were always below 500, which is also true for gas-heavy crude oil systems. For this range of N_f number, it was already observed that the flow field is axisymmetric, with particular relevance in the wake region (Campos and Guedes de Carvalho, 1988). For all simulated systems, the domain had a length 11 times larger than the tube diameter.

The starting meshes used to achieve the numerical results consisted on 52×1144 or 104×2288 quadrilateral control volumes distributed uniformly. Whenever necessary, extra refinement was applied in a region enclosing the single bubble tail or the leading bubble tail, in the simulations with two consecutive bubbles. The motivation behind this refinement is the elimination of a continuous liberation of small gas amounts, from the cusp-shaped region of the interface in the bubble tail, a numerical phenomenon that is attenuated by grid refinement. In this region, the meshes density can be four or 16 times higher than the initial one, depending on the number of refinements performed. In Fig. 1, a section of the original 104×2288 grid and also of a refined mesh (with one level of refinement) are shown. The mesh volume elements had an aspect ratio of approximately one, with the purpose of achieving a high level of accuracy and grid independence of the geometric reconstruction of the gas–liquid interface.

The procedure for defining the initial conditions of the gas volume fraction (α_G) depended if the intention was to simulate a system with a single Taylor bubble or a pair of consecutive bubbles. For the systems with an isolated bubble, the shape of the interface was initialized with a quarter of a circle, matching the region of the bubble nose, attached to a rectangular body with a width equal to the nose region radius. Other simpler initial shapes could lead to the same final results, but this geometry ensured a faster convergence on reaching a steady bubble shape. The initial values given to the film thickness, which defines the width of the rectangular body, were always based on the following equation (Brown, 1965):

$$\delta = \left[\frac{3\nu}{2g(R-\delta)}(U_{SB}(R-\delta)^2 - U_{SL}R^2)\right]^{1/3} \tag{4}$$

Once the final shape of a single Taylor bubble was achieved, it could be the base for the α_G initial condition in the simulations with a pair of consecutive bubbles. The gas volume fraction and the velocities – axial (u_z) and radial (u_r) – fields, obtained for an isolated bubble, were duplicated below the bubble tail at a separation distance of 75% of the L_{min} (minimum stabilization length below the bubble tail for single Taylor bubbles). This procedure led to the creation of a data file with new α_G, u_z and u_r fields that were used to start-up the simulations with two consecutive Taylor bubbles, i.e., two identical shaped bubbles separated by a previously defined initial distance (d_{in}).

Throughout this work, it was used a frame of reference attached to the isolated or to the leading Taylor bubble (MFR). This frame of reference implies that the tube wall moves downward at a velocity (U_{wall}) equal to the bubble rise velocity (U_{SB}). A no-slip condition was also assumed on the tube wall. An inlet flow boundary was used at the top of the domain by setting, in the stagnant liquid simulations, an inflow of liquid entering with a velocity equal to the single bubble or the leading bubble velocity in a fixed frame of reference ($U_{in} = U_{SB}$). Regarding the case of co-current liquid flow, the velocity profile used at this inlet boundary takes into account the parabolic profile for fully developed laminar flow in a pipe – $U_L(r)$ – and the corresponding single bubble velocity:

$$U_{in} = U_{SB} - 2U_{SL}\left[1 - \left(\frac{r}{R}\right)^2\right] \tag{5}$$

On the axis of the tube, zero normal gradients were assumed for all variables (symmetry boundary conditions). At the bottom of the computational domain, since the domain is sufficiently long to ensure the restoring of the inlet velocity profile, it was used an outflow boundary condition.

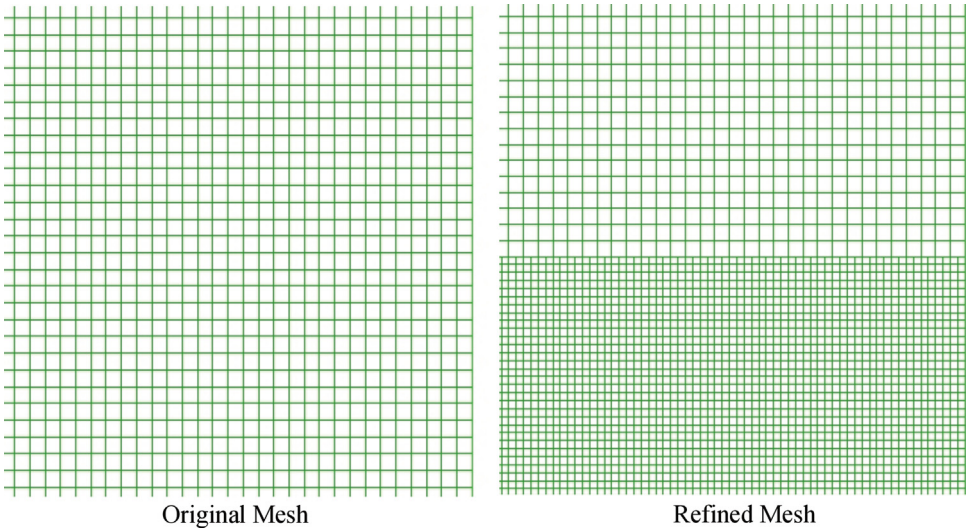

Fig. 1. Small section of the starting and refined meshes used in the simulations; starting mesh – $\Delta z = \Delta r = 1.54 \times 10^{-4}$ m; refined zone – $\Delta z = \Delta r = 3.85 \times 10^{-5}$ m.

When the flow of a single Taylor bubble is being simulated, the value of U_{SB} in the wall and inlet boundary conditions is changed until the bubble nose becomes stationary, meaning that it was found the correct value of the rise velocity. For each simulated flow condition, concerning the cases with stagnant liquids, the initial guess of U_{SB} was its experimental value (Campos and Guedes de Carvalho, 1988; Nogueira et al., 2006a). To obtain the numerical value of the single bubble velocity in the co-current system studied, the first estimate of U_{SB} was the result expected by the equation defined in the work of Nicklin et al. (1962):

$$U_{SB} = C_1 U_{SL} + U_0 \tag{6}$$

where U_0 is the single bubble velocity in a stagnant fluid, and C_1 is a constant that depends on the liquid velocity profile ahead of the bubble, which assumes, for laminar pipe flow, a value of approximately 2. It is important to notice that an expression equivalent to Eq. (6) is the base for drift-flux models which are extensively used to simulate multiphase flows in oil wells (Shi et al., 2005a, 2005b). Even though these models properly describe the slip between phases in a simple and continuous way, it is implicitly assumed a flow in fully-developed state and it is not included any feature about bubble–bubble interaction. A fully-developed state in continuous slug flow implies a stabilization of the liquid slug lengths distribution which can only occur at very large pipe lengths downstream the formation of this flow pattern.

Regarding the simulations with a pair of consecutive bubbles, the final numerical result of U_{SB} obtained for a single bubble, in similar flow conditions, was adopted into the wall and inlet boundary conditions. This assumption proved to be acceptable, since the position of the leading bubble nose was stable throughout both simulations.

The boundary and initial conditions just described and applied to the simulations with single bubble and two bubbles are sketched in Fig. 2.

The ANSYS FLUENT software offers two types of solvers: pressure-based and density-based. In both, a finite volume methodology is used to discretize the equations. However, in this CFD package, the VOF model can be used only with the pressure-based solver. The PISO (pressure-implicit with splitting of operators) was the pressure–velocity coupling scheme employed, which offers a more efficient calculation and faster convergence rates than the other SIMPLE family schemes, particularly for transient problems. The PISO scheme uses the pressure-based segregated algorithm where the governing equations are solved in a sequential manner. The pressure interpolation method applied was the pressure staggering option (PRESTO!), and the momentum equation was solved by the QUICK scheme. The Green-Gauss node-based method was used to compute the gradients of scalars, since it is known to be more accurate than the cell-based method.

The volume fraction equation was solved by an explicit time-marching scheme with a maximum Courant number of 0.25, and its spatial discretization was based on the geometric reconstruction approach. This discretization method is recommended for numerical codes involving VOF, since it is very accurate and produces better defined interfaces without numerical diffusion. Since the systems under study include gravity forces acting on phases with high density difference, segregated algorithms can experience convergence issues unless some measures are taken.

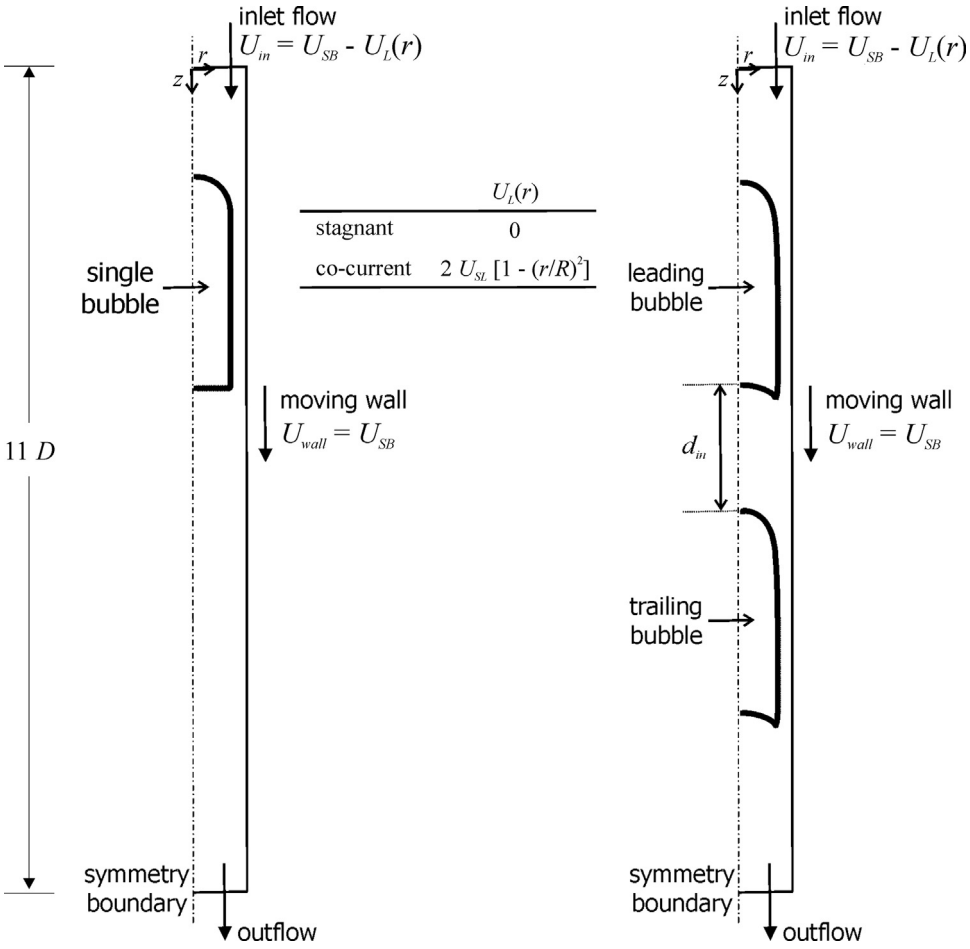

Fig. 2. Schematic representation of the domain, boundary and initial conditions for the simulations with single bubble (left side) and a pair of consecutive bubbles (right side).

For that purpose, the optional implicit body force treatment already implemented in the ANSYS FLUENT package was used.

The governing equations were solved with a variable time step that depended on a global Courant number fixed to 0.25, and each time step was limited to a maximum number of iterations of 1000. Also for each time step, the convergence criterion applied was based on the scaled absolute values of the axial and radial velocities and continuity residuals, which were all set to a maximum of 10^{-6}.

3. Results and discussion

Some essential grid density tests are first presented in this section. These tests were necessary to define the density of the meshes to apply, but the conclusions taken can also be important for studies with a scope larger than the one of the present work.

A validation study on the applicability of the numerical code to simulate slug flow systems is presented afterwards. With this purpose in mind, the motion of an isolated Taylor bubble through stagnant liquid was simulated under operating conditions already studied experimentally by Campos and Guedes de Carvalho (1988) and by Nogueira et al. (2006a). The tube diameter and relevant dimensionless groups that characterize the simulated conditions are presented in Table 1. The liquid phase consisted of aqueous glycerol solutions, and the gas phase was air. Comparisons were made between the available experimental results and numerical data obtained in this study, regarding the three main flow regions – near the bubble nose, developed liquid film and wake region.

Finally, the interaction between a pair of consecutive Taylor bubbles as they rise inside a vertical column of stagnant and co-currently flowing liquid (with an average velocity of 0.2 m/s) was simulated. The fluid properties defined for condition A of Table 1 were also applied to these simulations involving bubble–bubble interaction. The evolution of some hydrodynamic features throughout the bubbles approach process is presented in the last sub-section. The main purpose is to provide some detailed data about the less extensively studied scenario that consists of two consecutive Taylor bubbles rising through stagnant and co-current liquid, which can also be very useful as a preliminary study to its application to some practical situations, with particular interest on the petroleum industries. A relevant fact to support this interest is that the corresponding values of Morton and Eötvös numbers under study can also characterize some systems of gas-heavy crude oil flowing inside oil wells, and so, the conclusions and data taken in this work, about the hydrodynamics of Taylor bubbles interaction in a co-current liquid environment, should also be valid as a first step to improve the understanding and modeling of continuous slug flow in such scenarios occurring in oil plants. For example, considering a gas–oil system at a temperature around 38 °C, pressure in the range of 2000–3000 psi, composed by an oil with an API gravity around 18 – heavy oil according to the classification of De Ghetto et al. (1994) – and a gas–oil ratio (R_s) up to 15 m^3/m^3, with the help of some correlations to estimate surface tension and live oil viscosity (Standing, 1947; Kartoatmodjo and Schmidt, 1994;

Table 1
Tube dimensions and relevant dimensionless groups.

Condition	A[a]	B[a]	C[b]	D[b]	E[b]
D (m)	3.2×10^{-2}	3.2×10^{-2}	1.9×10^{-2}	1.9×10^{-2}	1.9×10^{-2}
N_f	111	201	205	325	483
M	4.31×10^{-2}	0.38×10^{-2}	1.44×10^{-4}	2.19×10^{-5}	4.28×10^{-6}
Eo	185.8	183.6	63.3	62.4	61.7

[a] Nogueira et al. (2006a).
[b] Campos and Guedes de Carvalho (1988).

Table 2
Values of U_{SB} and δ for different grid densities.

Condition	Grid	U_{SB} (cm/s)	δ (mm)	Error – U_{SB} (%)	Error – δ (%)
A	26×572	17.188	3.698	0.128	1.013
	52×1144	17.217	3.729	−0.041	0.192
	104×2288	17.210	3.736	–	–
B	26×572	17.995	3.149	0.272	0.929
	52×1144	18.045	3.170	−0.006	0.262
	104×2288	18.044	3.178	–	–

Abdul-Majeed and Abu Al-Soof, 2000), it was verified that the referred dimensionless numbers achieve values in the range of 1.2×10^{-1} to 1.3×10^{-2} and 220–330, respectively for M and Eo, which is fairly close to the ones obtained for condition A of Table 1.

3.1. Grid density tests

The first step to take was the definition of a standard grid density to produce mesh independent results throughout the set of simulations to perform. Three uniform meshes – 26×572; 52×1144; and 104×2288 elements – were tested by simulating the flow of a single Taylor bubble, in operating conditions experimentally studied by Nogueira et al. (2006a), and comparing some relevant results.

Primarily, the focus was placed on two important features – bubble rising velocity (U_{SB}) and developed liquid film thickness (δ). In Table 2, U_{SB} and δ values obtained for the different meshes are compiled together with the corresponding deviations. The reference mesh for these deviations was the denser grid (104×2288 elements). The operating conditions taken from Nogueira et al. (2006a) correspond to the conditions A and B of Table 1.

Regarding only the deviations presented in Table 2, one could be tempted to assume that, even with the 26×572 mesh, the results are completely independent of the grid density. However, with the purpose of producing highly accurate numerical results, a more detailed analysis was performed to guarantee the selection of a proper grid density. Looking into the region ahead the bubble nose, profiles of the axial and radial velocities (u_z and u_r), obtained for the conditions A and B with the three different meshes, and for an iso-surface positioned $0.05D$ above the nose tip, are shown in Fig. 3. The profiles are represented in a fixed frame of reference (FFR).

As it can be seen, the velocity profiles in Fig. 3 are almost overlapped, with the exception of u_z for the less dense mesh, where near the symmetry axis a small detachment from the remaining is detected. Another important feature from Fig. 3 is the similarity between the profiles obtained for both conditions; this can be a preliminary indicator that the flow disturbance above the bubble nose, caused by the bubble displacement, is not significantly affected by changes in the system properties.

A quantification of the liquid flow rate imbalance (in MFR) between the available cross section of the fully developed film and the top of the domain was also made to evaluate grid performance. These liquid flow rates were calculated from the equations:

$$Q_{film} = \int_{R-\delta}^{R} u_z 2\pi r dr \tag{7}$$

$$Q_{inlet} = U_{SB}\pi R^2 \tag{8}$$

The values estimated for the imbalance between Q_{film} and Q_{inlet} are 2.3%, 0.7% and 0.2%, for the grids with 26×572, 52×1144 and 104×2288 elements, respectively. These values were averaged between the results obtained for conditions A and B, and represent a strong indicator that, with the less dense grid, the numerical

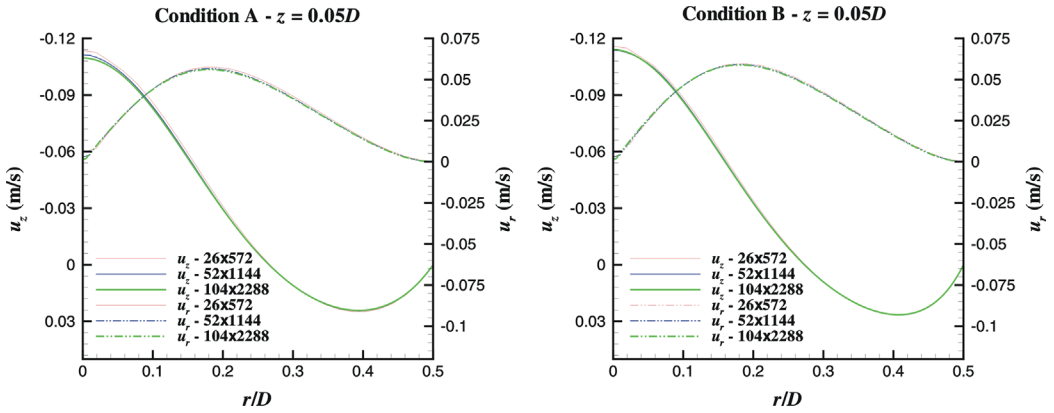

Fig. 3. Axial and radial velocity profiles (for a fixed frame of reference) for an iso-surface in the z coordinate placed 0.05 diameters above the bubble nose, obtained by simulation of conditions A and B (Nogueira et al., 2006a) using the three meshes under test.

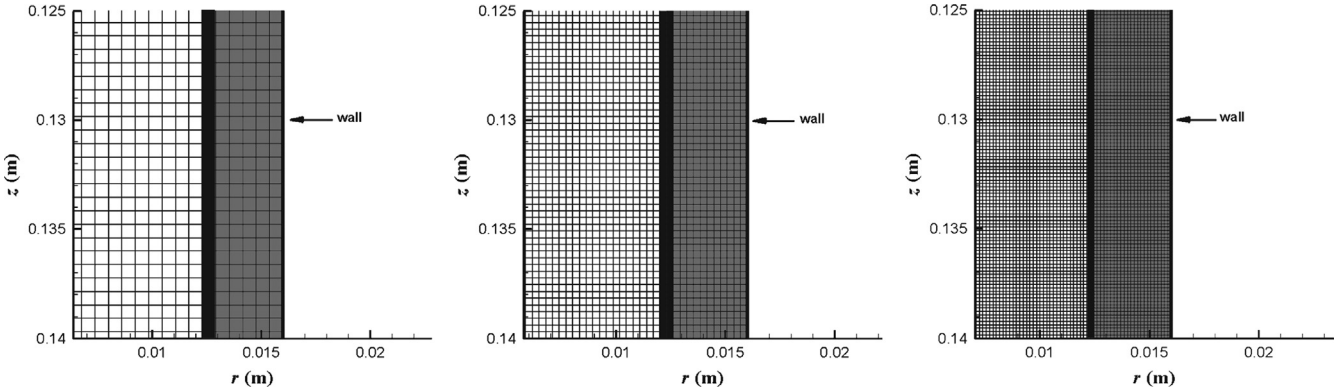

Fig. 4. Mesh representation and numerical results of the liquid phase volume fraction in a region near the developed liquid film obtained for condition A (Nogueira et al., 2006a), using the grids with 26×572, 52×1144 and 104×2288 elements (from the left graph to the right graph). Black color indicates the gas–liquid interface, white color represents liquid volume fraction of zero (at the left of the interface), and at gray color the liquid volume fraction is one (at the right of the interface).

data in the liquid film is inaccurate. Clearly, this is a consequence of an insufficient number of nodes/elements in the radial direction, describing the developed film region, as it is easily perceptible in Fig. 4.

From the observation of Fig. 4, it can be seen that for the 26×572 mesh the liquid film thickness only contains 6 nodes. The simulation data gathered for condition A was used to build these illustrations since it is characterized by a liquid film thickness higher than the one obtained for condition B, which implies that the number of nodes inside the film is even smaller for the latter flow condition. Related to a reduction of the size of each mesh element, in Fig. 4, it is also perceptible a reduction of the width of the numerical gas-liquid interface with an increase of the mesh density.

Since it is advisable a minimum of 10 nodes inside the liquid film, in the radial direction, this important factor forced the idea that grids with at least 52×1144 elements should be applied. Furthermore, since this work deals with systems characterized by small film thicknesses and Froude numbers above 0.30, the combination of these two features leads to high levels of u_z in the liquid film, which implies an increased risk of flow rate imbalance, and so, extra care was taken by deciding to use meshes of 104×2288 elements despite the increase of computational effort.

3.2. Validation of the computational code

The motion of an individual Taylor bubble through stagnant liquid was simulated for the operating conditions pointed out in Table 1, and experimentally studied by Campos and Guedes de Carvalho (1988) and Nogueira et al. (2006a), with the goal of validating the application of the CFD package to this kind of flow pattern.

Detailed post-processing analysis of these simulations was performed, and the numerical data, obtained using a mesh with 104×2288 elements, were compared with the experimental results. The most relevant hydrodynamic features are presented in the current section.

3.2.1. Bubble velocity and liquid film thickness

In Table 3 the numerical and experimental values of U_{SB} and δ (Nogueira et al., 2006a), for flow conditions A and B, are presented together with theoretical predictions. The deviations of the numerical results from experimental and theoretical values are also shown.

The theoretical values of the Taylor bubble velocity were calculated by a correlation defined in the work of Viana et al. (2003) and presented below:

$$Fr = \frac{0.34/(1+3805/Eo^{3.06})^{0.58}}{\left(1+\left(\frac{R_G}{31.08}\left(1+\frac{778.76}{Eo^{1.96}}\right)^{-0.49}\right)^{-1.45\left(1+\frac{7.22\times10^{13}}{Eo^{9.93}}\right)^{0.094}}\right)^{0.71\left(1+\frac{7.22\times10^{13}}{Eo^{9.93}}\right)^{-0.094}}} \quad (9)$$

where $R_G = \sqrt{D^3 g(\rho_L-\rho_G)\rho_L}/\mu_L$.

The predicted film thickness was based on Eq. (4), using the bubble rising velocity obtained by simulation.

The simulation results of U_{SB} and δ are closer to the theoretical values than to the experimental ones, and the numerical film

thickness shows even more accuracy than the bubble velocity when compared with the experimental data (maximum deviation of 8.46% for U_{SB} and 2.81% for δ). All the deviations obtained are within a very acceptable range (below 10%), and it is very significant to notice that the numerical values of U_{SB} present deviations smaller than 1%, when compared with the predictions of Viana et al. (2003).

Table 3
Numerical, experimental and predicted values of U_{SB} and δ, for flow conditions A and B, together with respective deviations.

	Simulation	Experimental	Theoretical
Condition A			
U_{SB} (cm/s)	17.21	18.80[a]	17.12[b]
|Error U_{SB}| (%)	–	8.46	0.54
δ (mm)	3.73	3.84[a]	3.74[c]
|Error δ| (%)	–	2.79	0.21
Condition B			
U_{SB} (cm/s)	18.04	19.70[a]	18.17[b]
|Error U_{SB}| (%)	–	8.41	0.72
δ (mm)	3.18	3.27[a]	3.16[c]
|Error δ| (%)	–	2.81	0.53

[a] Nogueira et al. (2006a).
[b] Viana et al. (2003).
[c] Brown (1965).

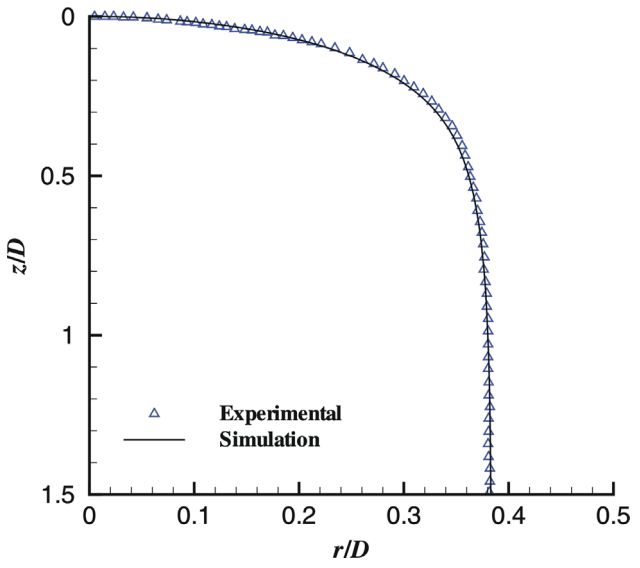

Fig. 5. Shape of the Taylor bubble in the nose region for the flow condition A: comparison between numerical (line) and experimental (symbols) data (Nogueira et al., 2006a). The axial and radial coordinates were used in a dimensionless form.

3.2.2. Shape of the bubble nose

The bubble shape in the nose region is also a relevant feature in the validation of the numerical code. The shape obtained in the simulation of an individual bubble under flow condition A is plotted in Fig. 5, together with the corresponding experimental data (Nogueira et al., 2006a).

From Fig. 5, it is proper to claim that the experimental data is predicted quite well by the simulation. The small deviations between the numerical and experimental values of δ (in the range of 3%) were already a strong indicator that pointed out to this conclusion.

Complementary comparisons between experimental data and simulations were performed using information retrieved from the work of Campos and Guedes de Carvalho (1988). A direct comparison between experimental and numerical bubble front ends was made for three conditions (C–E in Table 1). This comparison is presented in Fig. 6, where photos taken from the cited reference are placed in the background, and the interfaces at the bubble noses obtained by CFD are superimposed.

The superimpositions shown in Fig. 6 were performed only after the conversion of each photo and the corresponding numerical bubble interface to the same metric scale, with the purpose of producing meaningful comparisons. The radial boundary limit of the domain (column radius with 9.5 mm) and the reported experimental bubble lengths (Campos and Guedes de Carvalho, 1988), measured along the tube axis, were the scale references used for the referred conversions. As can be seen in Fig. 6, the front end bubble shapes obtained by simulation are almost a perfect match to the experimental observations. The only exception is the case of condition D, where the simulation seems to predict a nose with a larger contour than the corresponding photo. This probably results from some small errors (by defect) affecting the value of the experimental bubble length, which leads to a scale conversion that does not match exactly to the one of the related simulation.

3.2.3. Flow in the liquid film

Focusing in the fully developed film, the simulation results of δ were already addressed in Table 3. It is also relevant to infer the accuracy of the numerical results regarding the stabilized axial velocity profiles, and the related shear stresses along the liquid annulus. In Fig. 7, the numerical u_z profiles are plotted together with the corresponding experimental (Nogueira et al., 2006a) and theoretical data.

All the profiles shown in Fig. 7 were converted to a fixed frame of reference (FFR), and each one was normalized with the

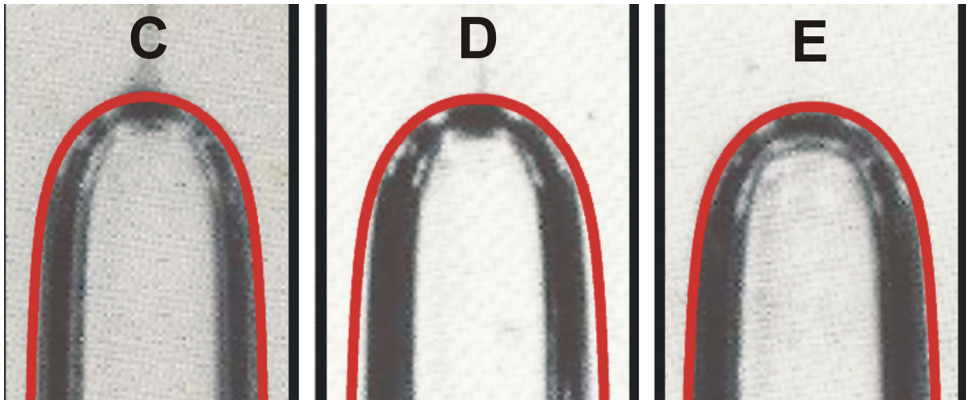

Fig. 6. Comparison between numerical and experimental (Campos and Guedes de Carvalho, 1988) Taylor bubble front ends for conditions C, D and E.

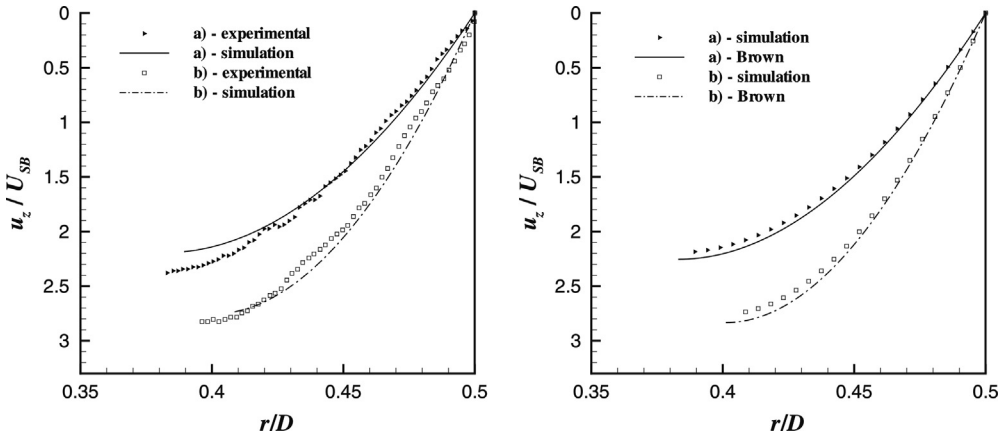

Fig. 7. Comparison of the axial velocity profiles in the fully developed film: simulation vs. experimental (on the left); and simulation vs. theoretical (on the right). The data presented corresponds to (a) condition A and (b) condition B.

corresponding value of U_{SB}. The normalization was performed to excel the general behavior of the u_z profiles, by eliminating the influence of the differences between experimental and numerical U_{SB} values, particularly noticed for radial positions near the bubble interface (where the instantaneous velocities are higher). The theoretical velocity profile was constructed with the help of an equation deduced by Brown (1965):

$$u_z = \frac{g}{\nu}\left[\frac{R^2 - r^2}{4} - \frac{(R-\delta)^2}{2}\ln\frac{R}{r}\right] \tag{10}$$

where δ is given by Eq. (4).

As depicted previously, the normalized simulation profiles (u_z/U_{SB}) are in a reasonable agreement with the experimental data. Even more conclusive than this, is the fact that the behavior of the same simulation profiles is predicted, by Brown's equation, with an excellent level of precision (right side of Fig. 7).

The shear stresses along the fully developed liquid film can be determined from the velocity profiles presented above, through the application of

$$\tau = -\mu_L \frac{du_z}{dr} \tag{11}$$

$$\tau_W = \frac{\delta(2R-\delta)}{2R}\rho g \tag{12}$$

The theoretical values of the wall shear stress were predicted by Eq. (12), for conditions A and B, and are presented in Table 4 together with the experimental values (Nogueira et al., 2006a) and the simulated ones. The numerical wall shear stresses are very close to the experimental values and theoretical predictions.

3.2.4. Flow in the wake region

For the majority of the conditions involving the flow of Taylor bubbles, when the liquid leaves the annular film, it creates a recirculation zone behind the bubble rear, which is generally known as wake region. Due to the significant influence of this flow region in the interaction between consecutive Taylor bubbles, it is crucial to gather detailed information about its flow pattern and hydrodynamic features.

The streamlines resulting from the simulation data for flow condition B are depicted in Fig. 8. These streamlines were obtained from the velocity vectors in a frame of reference moving with the bubble (MFR). As expected, the numerical streamlines reveal a laminar wake with a well defined recirculation zone inside, and the rear of the bubble exhibit a concave shape relative to the liquid phase. The experimental map of streamlines (Nogueira et al., 2006b) is also presented in Fig. 8. Besides the higher quality of

Table 4
Numerical, experimental and predicted values for the wall shear stress (τ_W).

	τ_W^{sim} (Pa)	τ_W^{exp} (Pa)	τ_W^{theor} (Pa)
Condition A	39.5	39.6	39.9
Condition B	33.6	32.3	34.2

the numerical vortex description, the experimental data in the recirculation zone is incomplete, since the measurement techniques were unable to determine the flow field inside the bubble rear concavity. These difficulties were due to an inefficient optical access, giving the illusion of a lower wake length when compared with the numerical predictions. This feature is another proof of the important increment that CFD techniques can give to hydrodynamic studies involving slug flow.

Similarly to what was previously presented for the nose region, a comparison between the numerical tail bubble shape and wake structure with the experimental information taken from the work of Campos and Guedes de Carvalho (1988) was performed. This comparison was made for the flow conditions C, D and E presented in Table 1. Based on the visualization of Fig. 9, it is fair to claim that the numerical bubble rear ends are an excellent fit to the experimental ones. Adding to the tail shape data, the amount of tracer visible in the photos of the experimental bubbles also enables a preliminary check regarding the quality of the numerical wake dimensions. The methodology applied to build Fig. 9 was similar to the one used for Fig. 6.

In order to characterize and quantify the flow in the wake of a Taylor bubble, two features are usually applied: the wake length (L_w) and the volume of the wake (V_w). For the flow conditions under study, the experimental and numerical results of the dimensionless wake length (L_w/D) and volume (V_w/D^3) are presented in Table 5, together with the corresponding deviations.

The procedure to determine these numerical features is supported on the assumption that the wake region is delimited by the bubble bottom and by the streamline that passes through the column centerline, in a region where the liquid flow is undisturbed by the Taylor bubble. After performing this delimitation, the corresponding volume can be obtained in the ANSYS FLUENT (Release 12.0.1), with the help of proper customized field functions. Knowing the axial position of the upper and lower limits of the wake region, placed in the column centerline, the corresponding length can be easily calculated as the difference between these two axial coordinates.

For conditions C, D, and E, the deviations between the experimental and numerical values of L_w/D and V_w/D^3, presented in

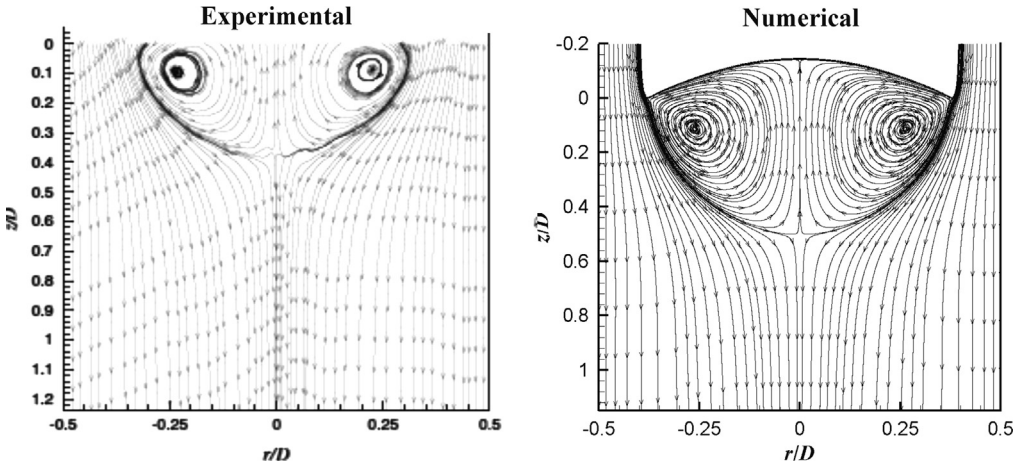

Fig. 8. Numerical and experimental (Nogueira et al., 2006b) streamlines in the wake of Taylor bubbles rising through stagnant liquid (MFR) for condition B. The origin of the axial coordinate (z/D) is placed at the tip of the bubble rear.

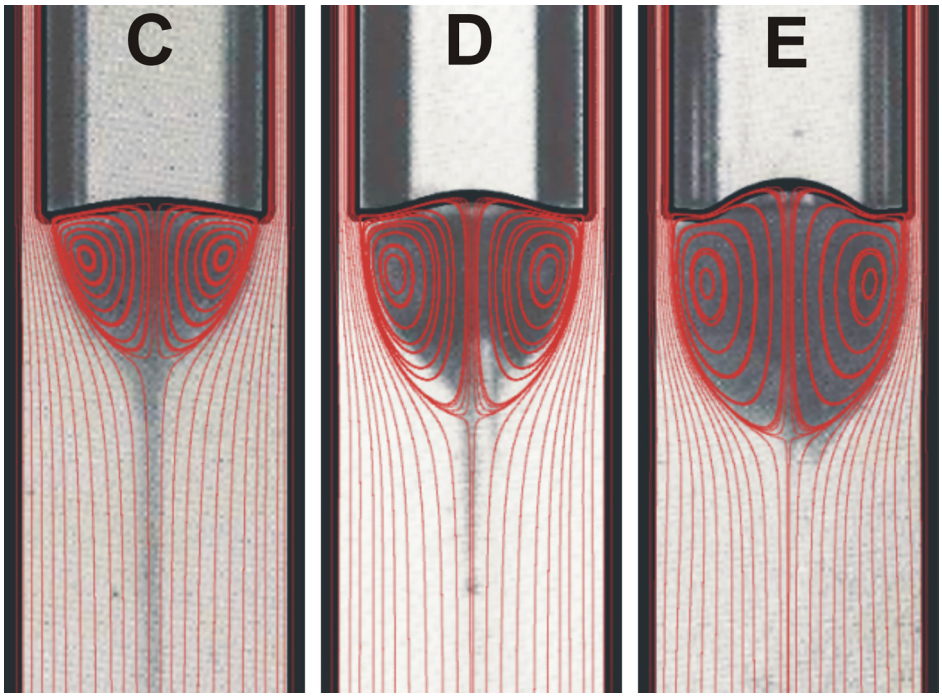

Fig. 9. Comparison between numerical and experimental (Campos and Guedes de Carvalho, 1988) Taylor bubble wakes for flow conditions C, D and E.

Table 5, reinforce the quality previously claimed, when discussing Fig. 9 regarding the numerical results of the wake length and volume. For these hydrodynamic features, the simulations were able to produce data deviated from the experimental results from 1% to 13%, which can be considered an error range fairly acceptable. However, for the two flow conditions studied by Nogueira et al. (2006b) – conditions A and B – the numerical results of L_w/D and V_w/D^3 have a large discrepancy when compared to the experimental values, with deviations between 40% and 50%. This can be justified by the fact that the experimental techniques applied by Nogueira et al. (2006b) do not take into account the portion of the wake inside the concavity of the bubble bottom, which systematically introduced errors by defect into the L_w and V_w experimental data determined by the referred techniques.

In conclusion, the information gathered throughout this validation section proves the reliability of the presented CFD model to simulate the rising of Taylor bubbles, in laminar regime, through columns filled with stagnant liquid. Exploring this fact, the application of this numerical code can be generalized to other configurations involving Taylor bubbles and a broader range of flow conditions, quantified by Morton and Eötvös numbers, in order to study their influence in the phenomenon under consideration.

3.3. Flow of two consecutive Taylor bubbles

Once the numerical code was validated in the previous subsection with data obtained for the rise of individual Taylor bubbles through stagnant liquids, the following step became the simulation of the flow behavior involved in the approach mechanism of a trailing bubble towards a leading one. For that purpose, a second bubble was added into the system concerning flow condition A (Table 1), and the approach process between the two bubbles was simulated in (1) stagnant liquid; (2) co-current liquid with an average velocity (U_{SL}) of 0.2 m/s. These simulations not only provide valuable data about the hydrodynamics in a system with a

Table 5
Numerical and experimental values of the dimensionless wake length (L_w/D) and volume (V_w/D^3), with respective deviations.

Condition	L_w/D	Error L_w (%)	V_w/D^3	Error V_w (%)
Simulation				
A	0.381	–	0.071	–
B	0.631	–	0.167	–
C	0.549	–	0.132	–
D	0.764	–	0.229	–
E	0.900	–	0.311	–
Experimental				
A[a]	0.190	−50.1	0.040	−43.7
B[a]	0.380	−39.8	0.091	−45.5
C[b]	0.544	−0.91	0.147	11.4
D[b]	0.667	−12.7	0.206	−10.0
E[b]	0.856	−4.89	0.342	9.97

[a] Nogueira et al. (2006b).
[b] Campos and Guedes de Carvalho (1988).

pair of consecutive Taylor bubbles, where there still exist a lack of detailed information, but more importantly, this data represents a first step to analyze in more detail the bubble interaction in "fundamental units" of continuous slug flow within systems characterized by dimensionless numbers that can also be found in several gas-heavy crude oil environments. Some relevant results obtained in the referred simulations are presented below.

Firstly, in both liquid flow configurations (stagnant and co-current), it is important to provide a qualitative overview on how the bubbles interaction influences the main hydrodynamic features, as the trailing bubble approaches the leading one. To achieve this goal, sequential images depicting simulation results of the gas–liquid interfaces and axial velocity fields, as the dimensionless separation distance (d/D) between bubbles gets shorter, are presented in Fig. 10. In this illustration, the axial velocity values were represented in a dimensionless form by using the corresponding leading bubble velocity (U_{SB}).

From the observation of Fig. 10, regarding the evolution of the bubbles shapes throughout the approach sequences, for both stagnant and co-current liquid, the only extremity that unquestionably remains undisturbed is the leading bubble nose. Besides, it is visible that this bubble extremity is sharper if the surrounding liquid is flowing co-currently when compared to liquid in stagnant state, leading also to thicker liquid films, which is in accordance to observations of previous studies (Nogueira et al., 2006a; Quan, 2011). Regarding the trailing bubble bottom, in both liquid flow configurations, it seems that its shape is approximately steady throughout the bubbles approach process, but a more detailed and quantitative analysis should be made in the future.

Briefly, as the trailing bubble approaches the bottom of the leading one, it displaces some of the liquid between them that must be drained through the film of the trailing bubble. This liquid drainage process experiences some flow resistance by the leading bubble bottom promoting a small but visible change in the curvature of this interface. It is also important to notice that, generally, the curvature of the bubbles tail is more pronounced with co-current liquid flow, which is again confirmed by previous literature (Nogueira et al., 2006a; Quan, 2011).

The bubble extremity that suffers the most noticeable shape alteration is the trailing bubble nose, particularly when it approaches the wake region of the leading bubble. In fact, for both liquid flow configurations, this extremity gets progressively sharpened but, as the separation distances (d/D) become very small, its behavior suddenly inverts and it begins to suffer an intense flattening. Accompanying this flattening, it is also relevant

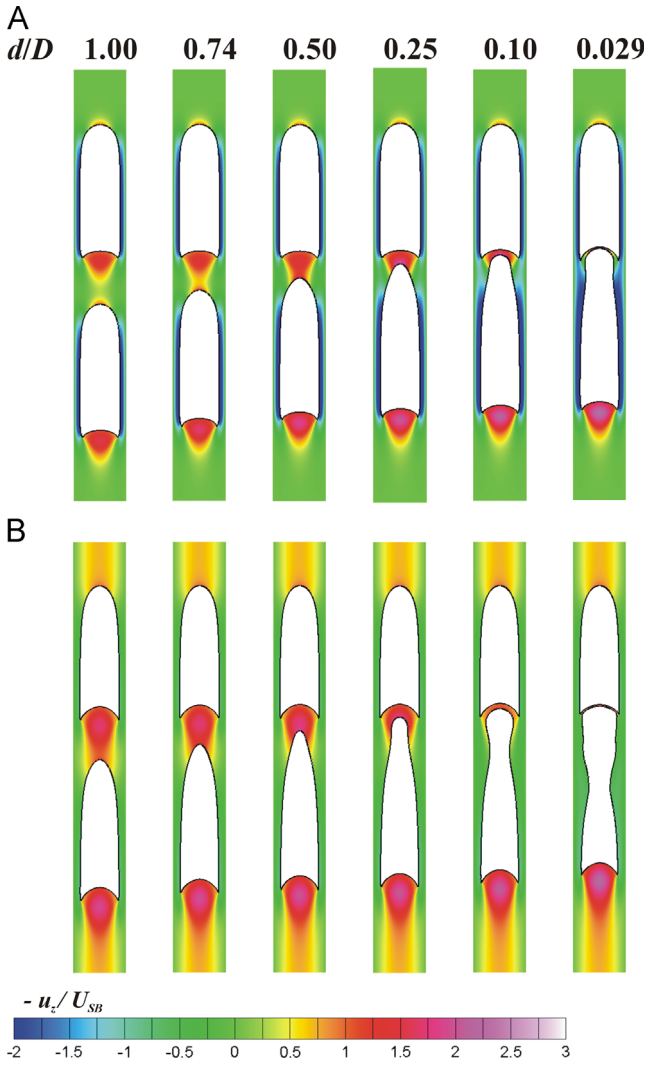

Fig. 10. Numerical data of the bubbles interface and axial velocity fields in the liquid phase, as the trailing bubble approaches the leading one, obtained for the simulations with stagnant (A) and co-current liquid (B). The separation distance is given in a dimensionless form (d/D), and the values of u_z are presented for a FFR (note that in this illustration the sign of the numerical results of the axial velocity is inverted, $-u_z$, for an easier perception of the upward direction of the movement of the bubbles and the liquid inside the wakes) and divided by the corresponding leading bubble velocity.

to refer the development of a neck-shaped zone in the body of the trailing bubble, just below its nose region. Furthermore, in the case of co-current liquid flow, this sharpening–flattening process is even more accentuated and develops faster, with the referred neck achieving smaller minimum thicknesses and dislocating to interface regions more distanced from the tip of the trailing bubble nose.

Concerning the dimensionless axial velocity fields illustrated in Fig. 10, a previous remark must be made: the numerical results of u_z were used in the FFR and their sign was inverted, in order to become more visible the real direction of the movement of the bubbles and the liquid inside the wake regions. The u_z field in the nose region and film of the leading bubble seems to be unchanged throughout the approach process, which is confirmed by the absence of displacement in the bubble nose tip verified during the simulation. On the contrary, the velocity field inside the wake region of the leading bubble is obviously dismantled from its initial shape, due to the liquid drainage from this region that is forced by the movement of the trailing bubble nose. During the major part of the bubbles approach process, the trailing bubble

nose encounters increasing velocity levels, immediately above of its tip, which should induce an accelerating movement to the trailing bubble, as it is later demonstrated. All of these preliminary observations regarding the u_z field can be verified in Fig. 10 for both stagnant (A) and co-current (B) liquid flow conditions.

Due to the already referred liquid drainage, both the developed film thickness (δ) and the u_z levels in the trailing bubble film increases, as d/D gets smaller, in order to accommodate the growing flow rate passing through this flow region. Although in the sequential images of Fig. 10 it is more perceptible for the stagnant liquid condition, the numerical results obtained for liquid flowing at U_{SL} of 0.2 m/s also confirm this u_z increase in the film region of the trailing bubble. In fact, since the U_{SB} value for the co-current configuration is around three times higher than the one for stagnant liquid, at first sight, the dimensionless u_z scale applied in Fig. 10 can induce to an incorrect interpretation in the specific feature of axial velocity inside the film region. To clarify this issue, despite the large differences encountered in the dimensionless u_z between stagnant and co-current liquid, the absolute values of the axial velocity inside the liquid films have similar magnitude and flow direction (downwards).

In order to confirm the important observations made in Fig. 10, regarding the growing tendency of the liquid film thickness (δ) of the trailing bubbles along the bubbles approach sequence, this hydrodynamic feature was quantified for several separation distances. For both liquid flow configurations, it was verified that it always increases as the bubbles get closer, which is mainly caused by the continuous downward drainage of the liquid present between the leading and trailing bubbles. To illustrate the magnitude of the variation in δ, a zoom of the film region of the trailing bubble is represented in Fig. 11 for two different moments – close to the beginning of the simulation, when the separation distance is one diameter; and for d/D of 0.029, when the bubbles are very near to coalesce. It should be noticed that the origin of the dimensionless axial coordinate was placed in the tip of the nose of the trailing bubble, and so, the vertical axis is the same for both moments in each flow configuration, although it can give the illusion of some displacement due to the stretching that the trailing bubble suffers when it gets closer to the leading one. A difference between the radial positions of the gas–liquid interfaces shown in Fig. 11 is notorious, which reflects a 13% and 17% increase in the liquid film thickness, for stagnant and co-current liquid, respectively, as the trailing bubble moves from a separation distance of 1.0D–0.029D. Due to the sharpening–flattening process already described, it should be referred that, when the separation distances were lower than 0.5, the simulation results for the co-current liquid condition revealed a trailing bubble with liquid film that was not fully developed, and so, the values of δ determined for this condition correspond to minimum thickness data. Although this is not totally accurate, the presented values of minimum film thickness should be an acceptable representation of the real values of δ.

Looking again to Fig. 10, for both stagnant and co-current liquid conditions, the axial velocity fields in the wake region of the trailing bubble reveal an apparent intensity increase, as the bubbles are approaching, which is a normal consequence since the liquid elements inside this region are accompanying a bubble that has an increasing rising velocity when compared to the leading one. It was also interesting to infer about the evolution of the wake dimensions (length and volume) during the approach process, and to quantify this data the methods already described in the previous sub-section were used. At the same two moments

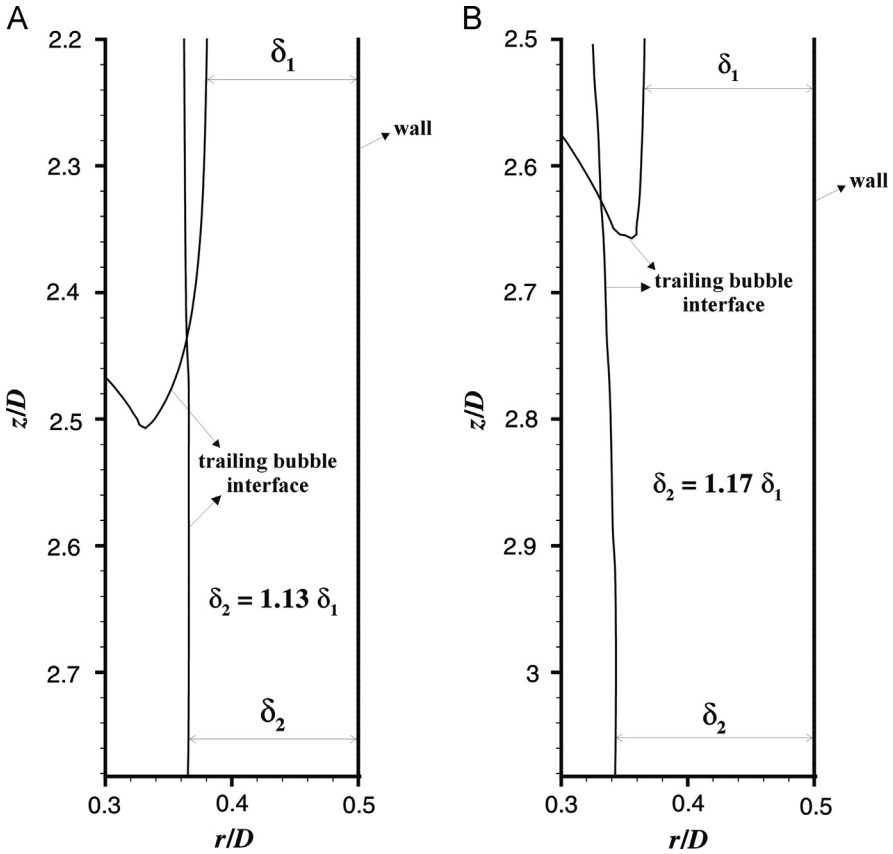

Fig. 11. Gas–liquid interface in the film region for the separation distances of 1.0D and 0.029D, corresponding to a liquid film thickness of δ_1 and δ_2, respectively, and obtained for the stagnant (A) and co-current liquid flow (B) simulations. The origin of the dimensionless axial coordinate (z/D) was placed in the tip of the nose of the trailing bubble.

chosen in Fig. 11, corresponding to separation distances of 1.0D and 0.029D, and for both flow configurations, a zoom was made to focus on the wake region of the trailing bubble and streamlines in the liquid phase surrounding the trailing bubble bottom were represented. For an easier perception of the wake region, shadows were also placed to signal the presence of this flow region, and the final illustration is shown in Fig. 12.

For the stagnant liquid condition, it is very clear that the wake region in the upper right image (d/D of 0.029) is larger than the one in the upper left image (d/D of 1.0). This visualization translates an increase of 30.3% and 36.6%, in the length and volume of the trailing bubble wake, respectively, as this bubble reduces the distance to the leading one from 1.0D up to a near coalescence scenario. However, when the liquid is flowing co-currently with a U_{SL} of 0.2 m/s, an opposite tendency is observed in the simulation results, i.e., the trailing bubble wake decreases its length and volume in 10.4% and 21.2%, respectively, as it moves from a distance to the leading bubble bottom of 1.0D to 0.029D. These opposing conclusions are most probably related to the relative importance of two factors: the increase of the average velocity of the liquid exiting the film of the trailing bubble; and the increase of the liquid film thickness. When the velocity of the liquid exiting the film increases, it should contribute to an expansion that needs a higher extent of liquid below the bubble bottom to recover to its original state, and so, an overall increase in the wake dimensions. On the other hand, if the film thickness is larger, the bubble maximum radius is lower and the available cross-section area for the liquid expansion is higher, which implies that it diminishes the influence length of this expansion, and so, the wake dimensions should decrease. Based on these ideas, it seems that: for the stagnant liquid condition, the role of velocity increase in the liquid film of the trailing bubble is more important, leading to a wake growth; and for the co-current liquid condition, the increase of the liquid film thickness of the trailing bubble is the controlling factor, which promotes a shrinkage of the wake as the bubbles are getting closer.

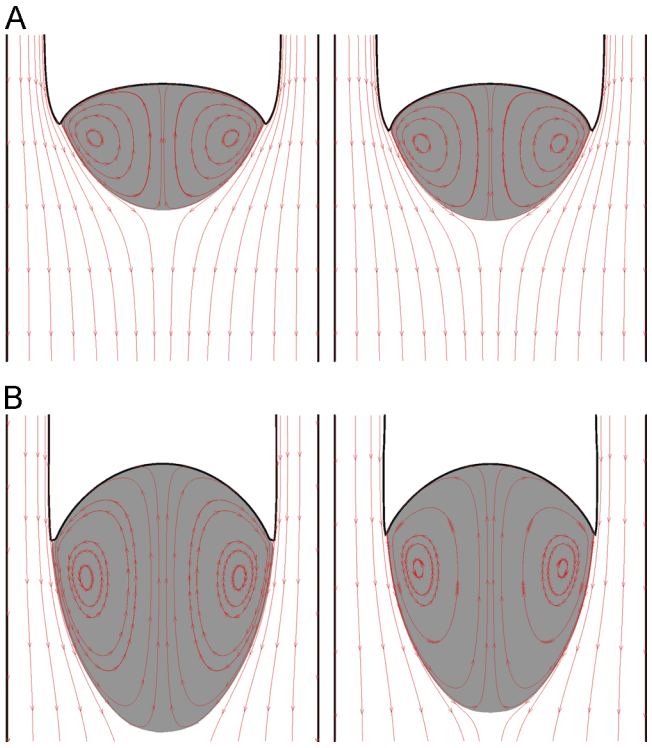

Fig. 12. Streamlines in the liquid phase surrounding the trailing bubble bottom for two separation distances between bubbles: 1.0D (left images) and 0.029D (right images). The upper row corresponds to numerical results obtained for the stagnant liquid condition (A), and the bottom row concerns the co-current liquid flow simulation (B) with a U_{SL} of 0.2 m/s. Shadows were placed to identify the wake region.

Finally, the most relevant hydrodynamic feature to characterize a system with a pair of Taylor bubbles rising through stagnant or co-current liquid is the velocity ratio (U/U_{SB}) between them. This ratio is determined by the displacement of the nose tip of the trailing bubble from a reference point placed in the leading bubble that must be previously defined. For consistency issues, since the distance between bubbles (d) is based on the positions of the tail of the leading bubble and of the nose of the trailing one, defined in the column axis, the tail of the leading bubble was used as reference point in the calculations of U/U_{SB}. For both liquid flow configurations, the behavior of the numerical results obtained for U/U_{SB}, as a function of d/D, is presented in Fig. 13.

Following the U/U_{SB} curves as the separation distance decreases, the velocity ratio continuously increases up to a maximum of 2.30 and 2.07, for stagnant and co-current liquid flow, respectively, occurring for d/D around 0.22 (stagnant liquid) and 0.38 (co-current liquid), and then decays abruptly to values near one as the bubbles are in the imminence of coalescence. To perform a deeper analysis of the velocity ratio data, an acceleration measure was defined by

$$\text{acceleration} = \frac{U}{U_{SB}} \frac{\partial(U/U_{SB})}{\partial(d/D)} \tag{13}$$

The results obtained by Eq. (13) have a behavior similar to the U/U_{SB} curve, exhibiting a maximum value at d/D of approximately 0.37 and 0.60, for stagnant and co-current liquid flow, respectively. This indicates that an approach process of the trailing bubble towards the leading one can be divided into an acceleration stage followed by a deceleration stage. The acceleration stage of the velocity ratio curves was already identified by several authors, and Moissis and Griffith (1962) stated that U/U_{SB} is a decreasing exponential function of the separation distance. The numerical data of U/U_{SB} presented in Fig. 13, regarding the acceleration stage, was adjusted to this kind of functionality, for both liquid flow conditions simulated, using two fitting parameters. The resulting equations concerning stagnant and co-current liquid flow simulations are presented below as Eqs. (14) and (15), respectively, and the corresponding curves are represented in Fig. 13 as solid lines.

$$\frac{U}{U_{SB}} = 1 + 4.35\exp\left(-4.03\frac{d}{D}\right) \tag{14}$$

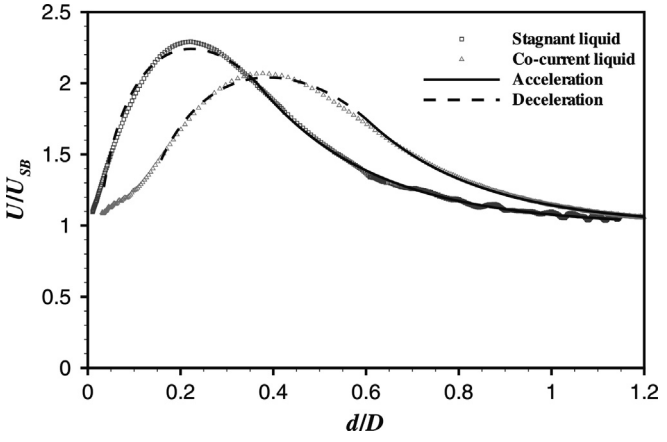

Fig. 13. Numerical results of the velocity ratio data (U/U_{SB}), as a function of the separation distance (d/D), gathered in the simulations of two consecutive Taylor bubbles for stagnant and co-current liquid flow (open symbols). The curves corresponding to the fitted equations obtained for the acceleration (solid lines) and deceleration (dashed lines) stages are also presented.

$$\frac{U}{U_{SB}} = 1 + 8.97\exp\left(-4.14\frac{d}{D}\right) \quad (15)$$

The deceleration region of the velocity ratio curves occurs at very small separation distances, and until now it was not addressed in published literature. To obtain a functionality that reasonably predicts the U/U_{SB} values in the deceleration stage, it was verified that the acceleration values in this stage, calculated by (13), are approximately described by a linear functionality with the natural logarithm of d/D. Based on this verification, the following equations were obtained to predict the numerical velocity ratio data in the deceleration stage, for the stagnant (16) and co-current liquid (17) flow simulations, using three fitting parameters:

$$\frac{U}{U_{SB}} = \sqrt{-1.11 - 41.08\left(\frac{d}{D}\right) - 27.42\left(\frac{d}{D}\right)\left[\ln\left(\frac{d}{D}\right) - 1\right]}; \quad 0.37 > \left(\frac{d}{D}\right) > 0.03 \quad (16)$$

$$\frac{U}{U_{SB}} = \sqrt{-4.71 - 21.44\left(\frac{d}{D}\right) - 22.76\left(\frac{d}{D}\right)\left[\ln\left(\frac{d}{D}\right) - 1\right]}; \quad 0.60 > \left(\frac{d}{D}\right) > 0.15 \quad (17)$$

It is very important to emphasize that the expressions gathered from (14) to (17) are also valid for the interaction between Taylor bubbles in gas–crude oil systems with Morton and Eötvös numbers around 4.31×10^{-2} and 186, respectively, under stagnant and co-current liquid flow with U_{SL} of 0.2 m/s. This kind of expressions are very helpful as an input to continuous slug flow simulators that can predict the evolution and distribution, along a pipe, of several hydrodynamic features such as the bubbles length and velocities, length of the liquid slugs and coalescence rate. It is a very good example on how detailed analysis with CFD techniques can complement and improve tools already useful in petroleum industry.

4. Conclusions

In this work, the dynamics of an individual and of a pair of consecutive Taylor bubbles rising in stagnant and co-current liquids, in laminar regime, was numerically investigated using a finite-volume numerical method (implemented in the commercial code ANSYS FLUENT-Release 12.0.1). The VOF methodology employed was the interface capturing technique. The computational results were consistently validated against detailed in-house measurements for the flow of a single Taylor bubble (Campos and Guedes de Carvalho, 1988; Nogueira et al., 2006a, 2006b). Careful grid density tests were performed in order to achieve the definition of a standard grid density generating mesh independent results.

For two flow conditions (A and B), simulation results of single Taylor bubble velocity were successfully compared with the values proposed by Viana et al. (2003) showing deviations under 1%, and the corresponding numerical data for the developed film thickness exhibited deviations from theoretical predictions (Brown, 1965) around 2.8%. These numerical results of U_{SB} and δ were also within a 10% deviation range from the reported experimental data (Nogueira et al., 2006a). Consistently with the accuracy in the predictions of the film thickness, for flow condition A, the numerically obtained bubble shape in the nose region compare quite well with the experimental one. To reinforce the validation on this flow region, numerical gas–liquid interfaces were superimposed on photos taken by Campos and Guedes de Carvalho (1988) and the match observed is very good. Regarding the flow in the developed liquid film, numerical data of the stabilized axial velocity profiles were favorably compared with experimental and theoretical results. A remarkable proximity was found between simulated wall shear stresses and both experimental and theoretical values. The flow in the recirculation zone behind the bubble rear, the wake region, was also carefully studied in the validation of the code applicability. For one of the flow conditions studied, the numerical map of streamlines was compared with the available experimental one, and two important issues must be emphasized: a higher quality of the numerical vortex description and a complete definition of the recirculation zone inside the bubble rear concavity, putting in evidence the important increment that CFD techniques can give to hydrodynamic studies involving slug flow. The wake volume and length were also numerically obtained to further characterize and quantify the flow behind an individual Taylor bubble. The accordance of these values with the available experimental and empirical data was once again reached within an acceptable range of agreement. The only exceptions concern the dimensions of the wake regarding the flow conditions (A and B) experimentally studied by Nogueira et al. (2006b), since it was previous knowledge that the techniques applied were not very effective to correctly determine this kind of hydrodynamic features.

After the validation of the numerical code applicability to slug flow was completed, it was successfully extended to a different flow configuration involving slug flow. Based on a flow condition already studied with a single Taylor bubble, in the validation section, two simulations were made by adding a second bubble to the system: one for stagnant liquid condition; and the other for co-current liquid flow with an average velocity of 0.2 m/s. The results obtained for this flow condition are also representative for gas-heavy crude oil systems, provided that the characterizing dimensionless numbers (M and Eo) are in the same order of magnitude. The expected bubble-bubble interaction was verified, and illustrative results of the influence of this interaction in some hydrodynamic features were presented. Regarding the bubble shapes, it was found that the most pronounced behavior changes, during the bubbles approach process, occur in the nose region of the trailing bubble. It starts from a sharpening tendency for higher separation distances that change to a flattening behavior and the appearance of a sort of a neck below the nose region. This sharpening-flattening process is more accentuated in the co-current liquid flow condition, where it starts earlier and presents thinner and longer necks. The bottom of the leading bubble also showed some shape variation, but not as drastic as the one found in the trailing bubble nose. The variation of the liquid film thickness and wake dimensions of the trailing bubble was also qualitative and quantitatively inspected. For the stagnant liquid condition, it was concluded that, although with different variation percentages, all of these features increase throughout the bubbles approach process. However, for the simulation with co-current liquid, as the trailing bubble gets closer to the leading one, its liquid film thickness increases but the wake dimensions shows a decrease. Finally, the velocity ratio between the bubbles was also determined as a function of the separation distance, for both liquid flow configurations, and the resulting curves revealed maximum values and two different stages on the movement of the trailing bubble towards the leading one – a period of acceleration and a deceleration stage. Equations were proposed to predict the U/U_{SB} values in these two stages, opening the possibility to be used as an input to continuous slug flow simulators applied in gas-crude oil systems.

Again, it is relevant to highlight that, due to the lack of detailed information about the effects of bubble-bubble interaction in the rising of two consecutive Taylor bubbles, this kind of CFD application should be the focus, in the future, of more systematic investigations, including conditions in turbulent regime. An immediate and important motivation is to determine more reliable and accurate data about bubble–bubble interaction in order to improve slug flow tracking simulators (Barnea and Taitel, 1993; van Hout et al., 2001; Mayor et al., 2007a, 2007b; Xia et al., 2009) or complement models

like the ones developed by Hasan and Kabir (2010a), Livescu et al. (2010) and Choi et al. (2013). The coupling of these computational and modeling tools can then be used to predict several hydrodynamic parameters inside oil wells and can help preventing some potential serious problems in the production facilities.

Acknowledgments

The authors gratefully acknowledge the financial support from the Foundation for Science and Technology (FCT) through the Project PTDC/EQU-FTT/69068/2006 and Grant SFRH/BPD/64148/2009. POCTI (FEDER) also supported this work via CEFT.

References

Abdul-Majeed, G.H., Abu Al-Soof, N.B., 2000. Estimation of gas–oil surface tension. J. Pet. Sci. Eng. 27, 197–200.
Aladjem Talvy, C., Shemer, L., Barnea, D., 2000. On the interaction between two consecutive elongated bubbles in a vertical pipe. Int. J. Multiphase Flow 26 (12), 1905–1923.
Angeli, P., Gavriilidis, A., 2008. Hydrodynamics of Taylor flow in small channels: a review. Proc. Inst. Mech. Eng. Part C J. Mech. Eng. Sci. 222 (5), 737–751.
Araújo, J.D.P., Miranda, J.M., Pinto, A.M.F.R., Campos, J.B.L.M., 2012. Wide-ranging survey on the laminar flow of individual Taylor bubbles rising through stagnant Newtonian liquids. Int. J. Multiphase Flow 43, 131–148.
Barnea, D., Taitel, Y., 1993. A model for slug length distribution in gas–liquid slug flow. Int. J. Multiphase Flow 19 (5), 829–838.
Brackbill, J.U., Kothe, D.B., Zemach, C., 1992. A continuum method for modeling surface tension. J. Comput. Phys. 100 (2), 335–354.
Branger, A.B., Lambertsen, C.J., Eckmann, D.M., 2001. Cerebral gas embolism absorption during hyperbaric therapy: theory. J. Appl. Physiol. 90 (2), 593–600.
Brill, J.P., Mukherjee, H., 1999. Multiphase Flow in Wells. Society of Petroleum Engineers Inc., Richardson.
Brown, R.A.S., 1965. The mechanism of large bubbles in tubes. I. Bubble velocities in stagnant liquids. Can. J. Chem. Eng. 43 (5), 217–223.
Bugg, J.D., Mack, K., Rezkallah, K.S., 1998. A numerical model of Taylor bubbles rising through stagnant liquids in vertical tubes. Int. J. Multiphase Flow 24 (2), 271–281.
Campos, J.B.L.M., Guedes de Carvalho, J.R.F., 1988. An experimental study of the wake of gas slugs rising in liquids. J. Fluid Mech. 196, 27–37.
Choi, J., Pereyra, E., Sarica, C., Lee, H., Jang, I.S., Kang, J.M., 2013. Development of a fast transient simulator for gas–liquid two-phase flow in pipes. J. Pet. Sci. Eng. 102, 27–35.
Chung, E.M.L., Hague, J.P., Evans, D.H., 2007. Revealing the mechanisms underlying embolic stroke using computational modelling. Phys. Med. Biol. 52 (23), 7153–7166.
Clanet, C., Héraud, P., Searby, G., 2004. On the motion of bubbles in vertical tubes of arbitrary cross-sections: some complements to the Dumitrescu–Taylor problem. J. Fluid Mech. 519, 359–376.
Clarke, A., Issa, R., 1997. A numerical model of slug flow in vertical tubes. Comput. Fluids 26 (4), 395–415.
Davies, R.M., Taylor, G., 1950. The mechanics of large bubble rising through extended liquids and through liquids in tubes. Proc. R. Soc. Lond. A 200 (1062), 375–390.
De Ghetto, G., Paone, F., Villa, M., 1994. Reliability analysis on PVT correlations. In: Proceedings of the SPE European Petroleum Conference. SPE 28904, London, United Kingdom, October 25–27.
Dumitrescu, D.T., 1943. Strömung an einer Luftblase im Senkrechten Rohr. Z. Angew. Math. Mech. 23 (3), 139–149.
Farhangi, M.M., Passandideh-Fard, M., Moin, H., 2010. Numerical study of bubble rise and interaction in a viscous liquid. Int. J. Comput. Fluid Dyn. 24 (1–2), 13–28.
Feng, J.Q., 2008. Buoyancy-driven motion of a gas bubble through viscous liquid in a round tube. J. Fluid Mech. 609, 377–410.
Goldsmith, H.L., Mason, S.G., 1962. The movement of single large bubbles in closed vertical tubes. J. Fluid Mech. 14 (1), 42–58.
Ha-Ngoc, H., Fabre, J., 2006. A boundary element method for calculating the shape and velocity of two-dimensional long bubble in stagnant and flowing liquid. Eng. Anal. Bound. Elem. 30 (7), 539–552.
Hasan, A.R., Kabir, C.S., 2010a. Modeling two-phase fluid and heat flows in geothermal wells. J. Pet. Sci. Eng. 71, 77–86.
Hasan, A.R., Kabir, C.S., 2010b. Simplified two-phase flow modeling in wellbores. J. Pet. Sci. Eng. 72, 42–49.
Hirt, C.W., Nichols, B.D., 1981. Volume of fluid (VOF) method for the dynamics of free boundaries. J. Comput. Phys. 39 (1), 201–225.
James, M.R., Lane, S.J., Chouet, B., Gilbert, J.S., 2004. Pressure changes associated with the ascent and bursting of gas slugs in liquid-filled vertical and inclined conduits. J. Volcanol. Geoth. Res. 129 (1–3), 61–82.
Kang, C.W., Quan, S., Lou, J., 2010. Numerical study of a Taylor bubble rising in stagnant liquids. Phys. Rev. E 81 (6), 066308.
Kartoatmodjo, F., Schmidt, Z., 1994. Large data bank improves crude physical property correlation. Oil Gas J. 4, 51–55.
Kawaji, M., DeJesus, J.M., Tudose, G., 1997. Investigation of flow structures in vertical slug flow. Nucl. Eng. Des. 175 (1–2), 37–48.
Liberzon, D., Shemer, L., Barnea, D., 2006. Upward-propagating capillary waves on the surface of short Taylor bubbles. Phys. Fluids 18 (4), 048103.
Livescu, S., Durlofsky, L.J., Aziz, K., Ginestra, J.C., 2010. A fully-coupled thermal multiphase wellbore flow model for use in reservoir simulation. J. Pet. Sci. Eng. 71, 138–146.
Lu, X., Prosperetti, A., 2009. A numerical study of Taylor bubbles. Ind. Eng. Chem. Res. 48 (1), 242–252.
Malekzadeh, R., Henkes, R.A.W.M., Mudde, R.F., 2012. Severe slugging in a long pipeline-riser system: experiments and predictions. Int. J. Multiphase Flow 46, 9–21.
Mayor, T.S., Pinto, A.M.F.R., Campos, J.B.L.M., 2007a. Hydrodynamics of gas–liquid slug flow along vertical pipes in the laminar regime – experimental and simulation study. Ind. Eng. Chem. Res. 46 (11), 3794–3809.
Mayor, T.S., Pinto, A.M.F.R., Campos, J.B.L.M., 2007b. Hydrodynamics of gas–liquid slug flow along vertical pipes in turbulent regime – a simulation study. Chem. Eng. Res. Des. 85 (11), 1497–1513.
Mercier, M., Fonade, C., Lafforgue-Delorme, C., 1997. How slug flow can enhance the ultrafiltration flux in mineral tubular membranes. J. Membr. Sci. 128 (1), 103–113.
Moissis, R., Griffith, P., 1962. Entrance effects in a two-phase slug flow. J. Heat Transfer 84 (1), 29–38.
Nicklin, D.J., Wilkes, J.O., Davidson, J.F., 1962. Two-phase flow in vertical tubes. Trans. Inst. Chem. Eng. 40, 61–68.
Nogueira, S., Riethmuler, M.L., Campos, J.B.L.M., Pinto, A.M.F.R., 2006a. Flow in the nose region and annular film around a Taylor bubble rising through vertical columns of stagnant and flowing Newtonian liquids. Chem. Eng. Sci. 61 (2), 845–857.
Nogueira, S., Riethmuler, M.L., Campos, J.B.L.M., Pinto, A.M.F.R., 2006b. Flow patterns in the wake of a Taylor bubble rising through vertical columns of stagnant and flowing Newtonian liquids: an experimental study. Chem. Eng. Sci. 61 (22), 7199–7212.
Pangarkar, K., Schildhauer, T.J., van Ommen, J.R., Nijenhuis, J., Kapteijn, F., Moulijn, J.A., 2008. Structured packing for multiphase catalytic reactors. Ind. Eng. Chem. Res. 47 (10), 3720–3751.
Pinto, A.M.F.R., Campos, J.B.L.M., 1996. Coalescence of two gas slugs rising in a vertical column of liquid. Chem. Eng. Sci. 51 (1), 45–54.
Pinto, A.M.F.R., Coelho Pinheiro, M.N., Campos, J.B.L.M., 1998. Coalescence of two gas slugs rising in a co-current flowing liquid in vertical tubes. Chem. Eng. Sci. 53 (16), 2973–2983.
Quan, S., 2011. Co-current flow effects on a rising Taylor bubble. Int. J. Multiphase Flow 37, 888–897.
Shemer, L., Gulitski, A., Barnea, D., 2007a. On the turbulent structure in the wake of Taylor bubbles rising in vertical pipes. Phys. Fluids 19 (3), 035108.
Shemer, L., Gulitski, A., Barnea, D., 2007b. Movement of two consecutive Taylor bubbles in vertical pipes. Multiphase Sci. Technol. 19 (2), 99–120.
Shi, H., Holmes, J.A., Durlofsky, L.J., Aziz, K., Diaz, L.R., Alkaya, B., Oddie, G., 2005a. Drift-flux modeling of two-phase flow in wellbores. SPE J. 10 (1), 24–33.
Shi, H., Holmes, J.A., Diaz, L.R., Durlofsky, L.J., Aziz, K., 2005b. Drift-flux parameters for three-phase steady-state flow in wellbores. SPE J. 10 (2), 130–137.
Sousa, R.G., Pinto, A.M.F.R., Campos, J.B.L.M., 2007. Interaction between Taylor bubbles rising in stagnant non-Newtonian fluids. Int. J. Multiphase Flow 33 (9), 970–986.
Standing, M.B., 1997. A pressure–volume–temperature correlation for mixtures of California oils and gases, *Drilling and Production Practice*. American Petroleum Institute, pp. 275–287.
Taha, T., Cui, Z.F., 2002. CFD modelling of gas-sparged ultrafiltration in tubular membranes. J. Membr. Sci. 210 (1), 13–27.
Taha, T., Cui, Z.F., 2006. CFD modelling of slug flow in vertical tubes. Chem. Eng. Sci. 61 (2), 676–687.
Talimi, V., Muzychka, Y.S., Kocabiyik, S., 2012. A review on numerical studies of slug flow hydrodynamics and heat transfer in microtubes and microchannels. Int. J. Multiphase Flow 39, 88–104.
van Hout, R., Barnea, D., Shemer, L., 2001. Evolution of statistical parameters of gas–liquid slug flow along vertical pipes. Int. J. Multiphase Flow 27 (9), 1579–1602.
Viana, F., Pardo, R., Yánez, R., Trallero, J.L., Joseph, D.D., 2003. Universal correlation for the rise velocity of long gas bubbles in round pipes. J. Fluid Mech. 494, 379–398.
White, E.T., Beardmore, R.H., 1962. The velocity of rise of single cylindrical air bubbles through liquids contained in vertical tubes. Chem. Eng. Sci. 17 (5), 351–361.
Xia, G.D., Cui, Z.Z., Liu, Q., 2009. A model for liquid slug length distribution in vertical gas–liquid slug flow. J. Hydrodyn. 21 (4), 491–498.
Youngs, D.L., 1982. Time-dependent multi-material flow with large fluid distortion. In: Morton, K.W., Baibnes, M.J. (Eds.), Numerical Methods for Fluid Dynamics. Academic Press, New York.
Zhang, H.Q., Wang, Q., Sarica, C., Brill, J.P., 2003. A unified mechanistic model for slug liquid holdup and transition between slug and dispersed bubble flows. Int. J. Multiphase Flow 29, 97–107.